Modeling and simulation of intersonic crack growth

Su Hao [a,*], Wing Kam Liu [a], Patrick A. Klein [b,*], Ares J. Rosakis [c]

[a] *Department of Mechanical Engineering, Northwestern University, 2154 Sheridan Road, Evanston, IL 60208, USA*
[b] *Sandia National Laboratories, Livermore, CA 94551, USA*
[c] *Division of Engineering and Applied Science, California Institute of Technology, Pasadena, CA 91125, USA*

Received 6 October 2003; received in revised form 6 October 2003

Abstract

Intersonic crack growth has been studied using an interfacial fracture model in which an additional material phase within a bonding layer is proposed to describe the failure behavior of the interface. In this material phase, a strain gradient based damage model is applied with a built-in cohesive law, which is governed by an material intrinsic length scale that bridges the mechanisms that operate at continuum mechanics scale and at smaller scales. Simulations of the intersonic crack growth experiments (Rosakis et al., 1999; Rosakis, 2002) have been performed with varying material length scales and other parameters. The study is focused on two subjects: (1) the process of decohesion-induced cracking, explaining fracture process zone initiation and propagation as well as the corresponding contact mechanisms; (2) propagation speed, investigating the effects of length scales and loading parameters.

The simulations reveal that a fracture process zone initiates first and extends with a speed faster than shear wave speed. After initiation, the crack speed exhibits oscillations with an average value between $c_s\sqrt{2}$ and c_1, where c_s and c_1 refer to shear wave and dilatation wave speeds, respectively. In such a quasi-steady-state propagation, the crack opening profiles exhibit a time-invariant profile, while the fracture process zone size and decohesion energy remain constant. Contact between the crack faces is taken into account in the numerical simulations. A contact zone behind the crack tip has been captured which represents a self-healing-like mechanism. The leading edge of both the fracture process zone and the contact zone may cause strong shocks. When the average crack propagation speed approaches the supersonic region, two stress shocks radiate from the crack tip, corresponding to shear and dilatation wave radiation, respectively. The simulation results demonstrate that length and time scales play vital roles during crack propagation. Here the length scales refer to the bonding layer thickness and the material's intrinsic length that governs energy dissipation during failure; whereas the time scales refer to the effects of material strain rate dependence, material failure speed, and wave propagation properties. A parameter R_s, expressed as the ratio of material shear strength and the applied stress that is calculated from the remote imposed displacement boundary condition, is proposed to scale crack speed. Intersonic propagation occurs when R_s is greater than a threshold value. The numerical computations are compared with experiments (Rosakis et al., 1999; Rosakis, 2002) and the theoretical solution [Philos. Mag., A, in press], which demonstrates the trend that crack propagation is unstable in the open speed interval between c_s and $\kappa_v c_s$

---

[*] Corresponding authors. Tel.: +1-847-4913046 (S. Hao), +1-925-2944618 (P. Klein).
E-mail addresses: suhao@northwestern.edu (S. Hao), w-liu@northwestern.edu (W.K. Liu), paklein@sandia.gov (P.A. Klein), rosakis@aero.caltech.edu (A.J. Rosakis).

($\sqrt{2} \leqslant \kappa_v < c_1/c_s$) whereas it is stable when the speed lies in the close interval between $\kappa_v c_s$ and c_1. The coefficient κ_v is a function of material length scale, strain rate sensitivity, and boundary conditions. The moving particle finite element method, a newly developed meshfree method, and the pinball contact algorithm are applied in the numerical analysis.

1. Introduction

The issues of the limiting speed of dynamic crack growth and the stress and strain fields surrounding a crack tip moving faster than the characteristic wave speeds have recently received a lot of attention (Rosakis et al., 1999; Rosakis, 2002). Washabaugh and Knauss (1994) find that the velocity of a mode I crack tip propagating along a fabricated weak plane may asymptotically approach the Rayleigh wave speed. The tests of mode II crack propagation along a weak plane conducted by Rosakis and his co-authors (Rosakis et al., 1999, 2000) reveal that given sufficient driving force, the crack propagation speed can jump to the intersonic speed regime, speeds lying between c_s and c_1, the shear and dilatational wave speeds, respectively.

The theoretical linear elastic dynamic crack growth analyses, as elegantly summarized by Freund (1990) and Broberg (1999a,b), indicate that the order of the stress singularity at such a crack tip and the corresponding energy release rate depends upon its propagation speed. For mode I crack growth in isotropic solids, the physically admissible stress singularity and the energy release rate vanish when the propagation velocity exceeds the Rayleigh wave speed. Whereas for mode II intersonic crack growth, the crack tip singularity is less than 1/2 which leads to a positive crack tip energy release rate. In this case, both the crack tip asymptotic solution (Freund, 1979) and dislocation analysis (Weertman, 1969; Weertman and Weertman, 1980) indicate that such a crack propagation is accompanied with stress radiation that has the same order as the crack tip stress except at the Eshelby speed, i.e. at $c_s\sqrt{2}$ where the corresponding crack tip singularity is 1/2. Griffith's Theory requires a crack tip stress singularity with a power of half. Thus, theoretically the Eshelby speed is the only admissible speed for steady-state mode II crack propagation above the shear wave speed.

On the other hand, both the analysis of seismic data (Bouchon et al., 2001) and experimental observations (Rosakis et al., 1999) demonstrate that a shear fracture on a pre-existing fault or a weak-path crack growth under mode II dynamic load can propagate in a wide range of speeds above the shear wave speed. A unified explanation is that the material decohesion in the weak path, rather than stress singularity, dominates the propagation under this situation, which actually smears out the stress concentration at the crack tip and thus removes the radiated stress singularity at shock front (Burridge et al., 1979; Broberg, 1999a,b; Needleman and Rosakis, 1999). From this view, several challenging issues are raised:

1. How does a crack initiate and grow from a static state to intersonic speeds?
2. When the Eschelby speed is no longer the uniquely admissible intersonic speed, which factors determine crack propagation speeds?
3. How does the material viscosity (strain rate sensitivity-drag effect) affect propagation?
4. What is the role of crack surface contact during decohesion and intersonic crack growth?
5. What are the effects of material intrinsic and extrinsic lengths on this class of problems?

Motivated by the Rosakis' experiment and seismological observations, a comprehensive numerical study focusing on the issues mentioned above is performed. As compared with previous research reports, the distinguishing points and contributions of the present work are as follows:

1. A three-phase model is proposed to simulate interface fracture, in which an additional interface material phase is introduced between two solid matrices in a bi-material system. The bonding strength and related mechanical properties are define by the constitutive law of this interfacial material phase.
2. The effects of length scales and strain rate have been investigated for the laboratory scale dynamic test. The length scales refer to the material intrinsic length presented in a strain gradient theory-based constitutive law whereas the extrinsic length refers to the bonding layer thickness that contains the interfacial phase.
3. In order to obtain the detailed information of intersonic crack propagation, the mode I and II crack opening displacements, the decohesion energy and fracture toughness are simulated and studied.
4. In conjunction with a multi-scale constitutive model (Hao et al., 2000c; Hao et al., in press), the moving particle finite element (Hao et al., 2002; Hao et al., in press), a newly developed numerical method, is applied in the simulations. Using this method we are able to
   • implement the contact mechanism into the numerical simulation. Several contact-related phenomena, such as self-healing, have been captured.
   • investigate some parameters and conditions that affect propagation speed which are currently difficult to simulate by other methods.
   • capture both intersonic and supersonic shocks, either in the stress or strain fields.
5. Both crack acceleration and deceleration have been studied. It has been found that the intersonic crack tip field radiates out from the site where a crack started to decelerate.
6. The numerical simulations are generally in agreement with the experimental observations (Rosakis et al., 1999; Rosakis, 2002) and theoretical predictions (Hao et al., in press) that intersonic crack propagation is unstable in the open speed interval between c_s and $\kappa_v c_s$ whereas it is stable when the speed lies in the close interval between $\kappa_v c_s$ and c_l. The parameter κ_v is a function of material intrinsic and extrinsic lengths, strain rate hardening parameters, and boundary conditions.

A considerable number of reports regarding intersonic and supersonic crack propagation can be found in the past three decades, including Andrews (1976), Burridge et al. (1979), Weertman and Weertman (1980), Piva and Hasan (1996), Huang et al. (1998), Gumbsch and Gao (1999), Huang et al. (1999), Needleman (1999), Needleman and Rosakis (1999), Ben-Zion (2001), Dwivedi and Espinosa (submitted for publication), Federici et al. (2001), Geubelle and Kubair (2001), Samudrala et al. (2002), Guo et al. (2003) and Samudrala and Rosakis (2003). Reviews of dynamic fracture in seismic studies are presented by Dmowska and Rice (1986) and Freund (1990), and recently by Rosakis (2002). With respect to numerical analysis, Andrews (1976) first simulated intersonic shear failure using a finite difference technique. Applying cohesive finite elements, Needleman and Rosakis (1999) study the effects of loading rate and strength of the weak path. Gumbsch and Gao (1999) simulate intersonic crack growth using molecular dynamics. Molecular dynamics simulations of supersonic crack propagation were conducted recently by Gao et al. (2001). The effects of strain rate sensitivity (drag) and strain gradient on single dislocation motion with speeds in subsonic, intersonic, and supersonic regions has been analyzed by Rosakis (2001). As an complement to this paper, a theoretical analysis of steady-state intersonic crack growth has been conducted in Hao et al. (in press) based on the moving dislocation solution introduced in Weertman and Weertman (1980).

This paper is organized as follows: Section 2 gives the problem statement, a brief introduction of the multi-scale damage constitutive law that is applied in the numerical simulation, and the proposed interface fracture model. The corresponding numerical scheme is illustrated in Section 3. The simulation results and discussions are presented in Section 4. Section 5 summarizes conclusions.

In the analysis that follows, boldface letters are used to represent tensors. Plan letters represents scalars. Plain letters with subscripts represent the components of a tensor, where the Einstein summation convention is applied to repeated subscripts.

2. Problem statement, interfacial fracture model, and constitutive law

2.1. Problem statement and experimental configuration

Caltech's mode II dynamic shear rupture specimen (Rosakis et al., 1999) is shown in Fig. 1. It is composed of two pieces of Homalite-100 (a photoelastic polymer) bonded along a horizontal interface. The bonding is produced by using the monomer of the photoelastic polymer and by polymerizing in situ using a catalyst. The resulting adhesive material has elastic properties that are very close to those of the two monolithic pieces and variable strength depending on the curing time. Its strength is in general lower than the monolithic Homalite, a condition necessary to trap the resulting shear crack and to force it to propagate along the weak bond without kinking into the Homalite pieces. Its height, h, is of the order of 100 μm. A notch is machined along the bond line. Asymmetric dynamic loading is provided by firing a steel projectile onto the upper half of the specimen just above the pre-notch. The impact velocities range from 20 to 35 m/s. The impacting projectile loads the notch in shear (a small component of compression is also present) and produces a concentration of shear stresses along the weak bond. As the shear stresses and strain rates increase at the notch tip, a dynamically growing shear rupture is produced and grows along the bond with intersonic speeds (Rosakis et al., 1999). The rupture process is visualized by means of high speed photography (2 million frames/s) and the optical method of photoelasticity. Photoelasticity, which is sensitive to
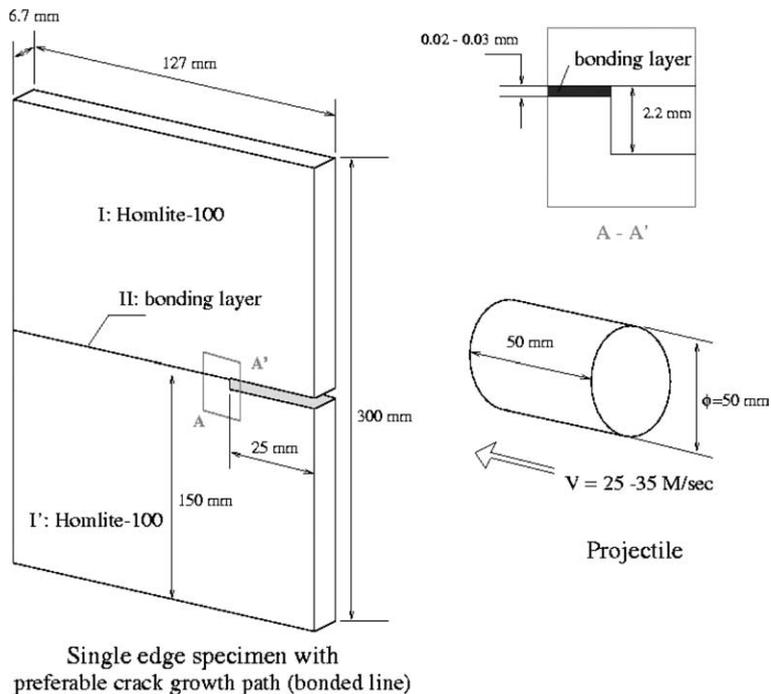
Fig. 1. Caltech mode II dynamic fracture test.

maximum shear stresses, is the ideal technique to be used in visualizing shear dominated fracture events. Indeed, the intersonic shear ruptures reported by Rosakis et al. (1999) are seen to feature two very well resolved shear shock waves (discontinuities in shear stress) that are attached to the intersonically moving shear crack tip, clearly revealing the intersonic nature of the dynamic shear rupture processes.

2.2. Three-phase interfacial fracture model

For the specimen shown in Fig. 1, the upper and lower solid domains are made of Homalite-100 (Rosakis et al., 1999). Instead of ideal bonding, we assume that a thin material layer with a height h exists between the two pieces. The bonding and decohesion properties are defined by the constitutive law that governs this third material, which will be described in the next subsection. Hence, interfacial debonding of the specimen shown in Fig. 1 is modeled as the fracture problem involving the sandwich structure shown in Fig. 2 with an additional length scale h, which is considered as a material "extrinsic length" for this model. In reality, such bi-material interfacial transition zones always exist at micro-scale due to the diffusions. According to experimental result, in the present analysis, the h is taken from 1 to 200 μm and its effect on intersonic crack growth has been studied. For the specimen shown in Fig. 1, it has been reported that h is about 20 μm (Rosakis et al., 1999; Rosakis, 2002).

2.3. Constitutive equation and length scale dependent cohesive law

In the present analysis, the bulk Homalite-100 is assumed to be isotropic and linearly elastic. The bonding layer phase is modeled by the multi-scale damage constitutive model introduced in Hao et al. (2000c) and Hao et al. (in press) that is described briefly as follows.

Assuming finite deformations but infinitesimal elastic strain, we apply the additive decomposition of the strain rate tensor

$$\dot{\varepsilon} = \dot{\varepsilon}^{\mathrm{e}} + \dot{\varepsilon}^{\mathrm{p}} \tag{1}$$

where $\dot{\varepsilon}^{\mathrm{e}}$, the elastic part of strain rate, obeys the same linear elastic constitutive law as the bulk Homalite-100. The plastic part of strain rate, $\dot{\varepsilon}^{\mathrm{p}}$, is described by the plastic potential:
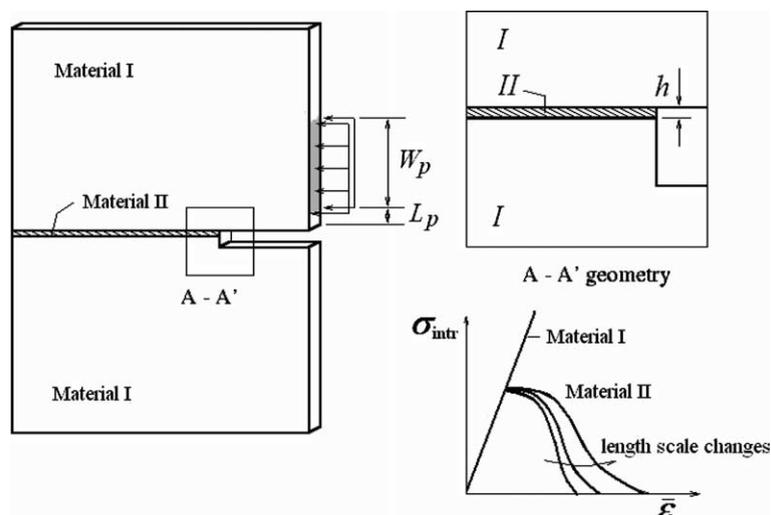
Fig. 2. A three-phase model for intersonic interfacial shear fracture.

$$\Phi_{\text{multi}} = \left(\frac{\overline{\sigma}}{\sigma_{\text{intr}}}\right)^2 + A_0\frac{\sigma_{\text{m}}}{\sigma_{\text{intr}}} + A_1(f + g_1)\exp\left(-\frac{\sigma_{\text{m}}}{\sigma_{\text{intr}}}\right) + A_2(f + g_2)\exp\left(\frac{\sigma_{\text{m}}}{\sigma_{\text{intr}}}\right) - (1 + qf^2) = 0 \tag{2}$$

and the associative flow rule

$$\dot{\boldsymbol{\varepsilon}}_{\text{p}}^{\text{p}} = \dot{\lambda}\frac{\partial\Phi_{\text{multi}}}{\partial\boldsymbol{\sigma}} \tag{3}$$

where $\dot{\lambda}$ is the "flow factor", $\overline{\sigma}$ and σ_{m} denote the Cauchy equivalent stress and Cauchy mean stress, respectively; f represents the void volume friction which is considered as a damage. The parameters A_0, A_1, A_2, g_1, g_2, and q are dimensionless material constants as listed in Table 1. The evolution laws of damage nucleation and growth introduced in Tvergaard and Needleman (1992) are applied in the present work. In Hao et al. (in press) a hierarchical constitutive model is developed that unions quantum physics with the sub-micro and micro-cell models in continuum mechanics. The relation (2) is derived based on the macro-scale potential obtained from micro-cell model.

The plastic potential (2) is associated with the multi-scale damage model in which the mechanisms from two scales are taken into account. At macro-scale up to the point of bifurcation, the J_2-like plasticity and damage in the form of void nucleation and growth are taken as the dominant mechanisms of failure, which is a combination of J_2-plasticity, the Rice–Tracey model (Rice and Tracey, 1969), and Coulomb friction. A computational methodology to calibrate the constants is introduced in Hao et al. (2000a). The collapse of the ligaments between voids or between other defects is considered as the mechanism after the onset of bifurcation, which highlights the underlying mechanisms at smaller scales which become dominant through global material failure. At this stage the matrix material is modeled by a set of material particles connected by a network of "virtual internal bonds" where each bond obeys the strain gradient-based localization solution that defines a traction-separation law [25]. The development of the micro-ligament collapse model, which is absent in the conventional Gurson's model, is based on the idea that combines the computational cell model, the concurrent two-scale simulation (Hao et al., 2000b), and the "virtual internal bond model" of cohesive material structure (Klein and Gao, 1998). For the isotropic case, the average stress–strain response of this model is described by σ_{intr} at macro-scale, which is named as "material intrinsic strength" in (2). It is defined as the combination of material strain hardening/softening law and the strain gradient-based traction-separation law:

$$\sigma_{\text{intr}} = \begin{cases} \overline{\sigma} \text{ strain hardening/softening,} & \overline{\varepsilon}^{\text{p}} \leqslant [\overline{\varepsilon}]^{\text{bifurc}} \\ T(\widetilde{Y}, l, \eta) \text{ decohesion softening,} & \overline{\varepsilon}^{\text{p}} > [\overline{\varepsilon}]^{\text{bifurc}} \end{cases} \tag{4}$$

where the $\overline{\varepsilon}^{\text{p}}$ is the plastic part of equivalent strain and $[\overline{\varepsilon}]^{\text{bifurc}}$ denotes the $\overline{\varepsilon}^{\text{p}}$ at the bifurcation point the on $\sigma_{\text{intr}}(\overline{\varepsilon}^{\text{p}})$ relation. l is the material intrinsic length scale defined as the product of Burger's vector b and the initial yield strength σ_{Y0}. η is the equivalent strain gradient (Gao et al., 1999):

$$l = 3\left(\frac{E}{\sigma_{Y0}}\right)^2 b; \quad \eta = \sqrt{\frac{1}{2}u_{k,ij}u_{k,ij}}$$

Table 1
The coefficients in (2)

A_0	A_1	A_2	g_1	g_2	q
0.0666	0	1.7	0	0	0.45
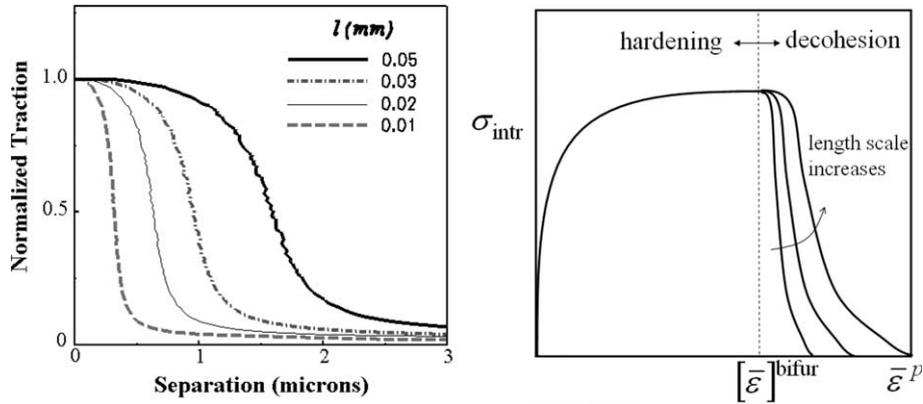
Fig. 3. The built-in cohesive law and the definition of material intrinsic strength.

and the strain-like parameter $\widetilde{Y}$ is defined by

$$\widetilde{Y} = (\bar{\varepsilon}^{\mathrm{p}} - [\bar{\varepsilon}]^{\mathrm{bifur}})\frac{l}{l_0} \tag{4a}$$

where l_0 is a material constant. As illustrated in Fig. 3, $[\bar{\varepsilon}]^{\mathrm{bifurc}}$ marks the transition between the two stages of deformation, the uniform deformation with damage nucleation and growth and the failure of the ligaments between these defects. $[\bar{\varepsilon}]^{\mathrm{bifurc}}$ can be calibrated to the maximum stress on the $\sigma_{\mathrm{intr}}(\bar{\varepsilon}^{\mathrm{p}})$ curve from the uniaxial tension test. During the second stage, the effect of the material intrinsic length scale, strain gradient, and strain rate are incorporated in σ_{intr} (4) as

$$T = \sigma_{Y0} \cdot \widetilde{T}(\bar{\varepsilon}^{\mathrm{p}}, l, l_0) \cdot \left(1 + \frac{\dot{\bar{\varepsilon}}}{\dot{\bar{\varepsilon}}_0}\right)^m \cdot \sqrt{\left[\frac{\sigma_{\mathrm{hom}}(\bar{\varepsilon}^{\mathrm{p}})}{\sigma_{Y0}}\right]^2 + l\eta} \tag{5}$$

The second term in (5) is the traction-separation law derived from the strain gradient-based localization solution at the micro-scale. The third and fourth terms reflect, in turn, the strain rate effect and the material hardening due to the strain gradient at macro-scale. As the micro-scale localization, representing ligament failure, is described by $\widetilde{T}$ in (5), the stress–strain response without bifurcation, denoted by $\sigma_{\mathrm{hom}}(\bar{\varepsilon}^{\mathrm{p}})$, appears under the square root of the fourth term.

Based on the analytical solution described in Hao et al. (2000b), $\widetilde{T}$ can be approximated as

$$\widetilde{T} = \frac{-0.5398Y^2 + 1.5867Y - 0.0466}{1 - k_{\mathrm{tr}}} \tag{5a}$$

where

$$Y = \exp\left\{10^6 \cdot (\widetilde{Y})^{\frac{11}{3}}\right\}; \quad k_{\mathrm{tr}} = \left|\frac{\sigma_I - 3\sigma_{\mathrm{m}}}{2\sigma_I}\right| \quad \text{and } k_{\mathrm{tr}} < 1$$

where σ_I is the maximum principle stress and k_{tr} represents the triaxiality of the stress state. In the cases of pure triaxial tension and compression ($k_{\mathrm{tr}} = 1$), it is assumed that the fine scale mechanism is not activated as no shear stress exists to trigger localization. As illustrated in Fig. 3, the primary effect of the material intrinsic length l is a scaling of the energy dissipated during decohesion.

For the numerical simulations we employed a bilinear approximation to (5a) that incorporates the essential characteristics in an expression with reduced complexity (see Fig. 4)
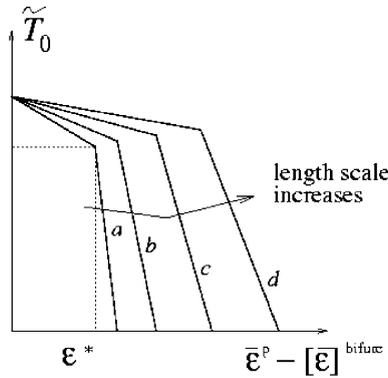
Fig. 4. The bilinear expression of the cohesive law and its variation with the material intrinsic length.

$$\widetilde{T}_0 = \begin{cases} 1 - \kappa_0\big(\bar{\varepsilon}^{\mathrm{p}} - [\bar{\varepsilon}]^{\mathrm{bifurc}}\big), & \bar{\varepsilon}^{\mathrm{p}} - [\bar{\varepsilon}]^{\mathrm{bifurc}} \leqslant \bar{\varepsilon}^* \\ \kappa_1 - \kappa_2\big(\bar{\varepsilon}^{\mathrm{p}} - [\bar{\varepsilon}]^{\mathrm{bifurc}}\big), & \bar{\varepsilon}^{\mathrm{p}} - [\bar{\varepsilon}]^{\mathrm{bifurc}} > \bar{\varepsilon}^* \end{cases} \tag{5b}$$

where

$$\kappa_0 = \frac{1}{\pi}; \quad \kappa_1 = \frac{1 - \bar{\varepsilon}^*/\pi}{1 - \sqrt{3}/2}; \quad \kappa_2 = \frac{1 - \bar{\varepsilon}^*/\pi}{\bar{\varepsilon}^*(2/\sqrt{3} - 1)}; \quad \bar{\varepsilon}^* = 0.041\frac{l}{l_0}$$

For a metal, it is suggested that $l_0 = 100\ \mu\mathrm{m}$ (Hao et al., in preparation).

3. Numerical scheme

3.1. Discretization and model parameters

Three-dimensional meshfree simulations have been performed using the configuration shown in Fig. 5a. The specimen is discretized into 2–5 layers in thickness direction. Each layer has about 11,000 nodes (total 5 layers) to 112,000 nodes (total 2 layers). The distribution of nodes in the vicinity of the notch tip is illustrated in Fig. 5b.

The impact of the projectile is modeled by two methods: the projectile is assumed to be a rigid body acting on the specimen; and the projectile is replaced by a prescribed velocity boundary condition. No significant differences are observed between the two approaches. The contact algorithm used with the rigid projectile requires additional computational effort. The fixed velocity boundary condition is imposed on the specimen edge along a height equal to the diameter of the projectile. The imposed velocity varies in time as described by Needleman (1999) and Needleman and Rosakis (1999):

$$\overline{V}_{\mathrm{p}}(t) = \begin{cases} V_{\mathrm{p}}t/t_i, & 0 < t < t_i \\ V_{\mathrm{p}}, & t_i \leqslant t \leqslant t_{\mathrm{p}} \\ V_{\mathrm{p}}[1 - (t - t_{\mathrm{p}})/t_{\mathrm{s}}], & t_{\mathrm{p}} \leqslant t \leqslant t_{\mathrm{p}} + t_{\mathrm{s}} \\ 0, & t_{\mathrm{p}} + t_{\mathrm{s}} \leqslant t \end{cases} \tag{6}$$

where V_{p} is the velocity of the projectile. In the present computation, t_i and t_{s} are chosen to be zero while t_{p} is equal to twice the time that a dilatational wave takes to travel the length of the projectile.
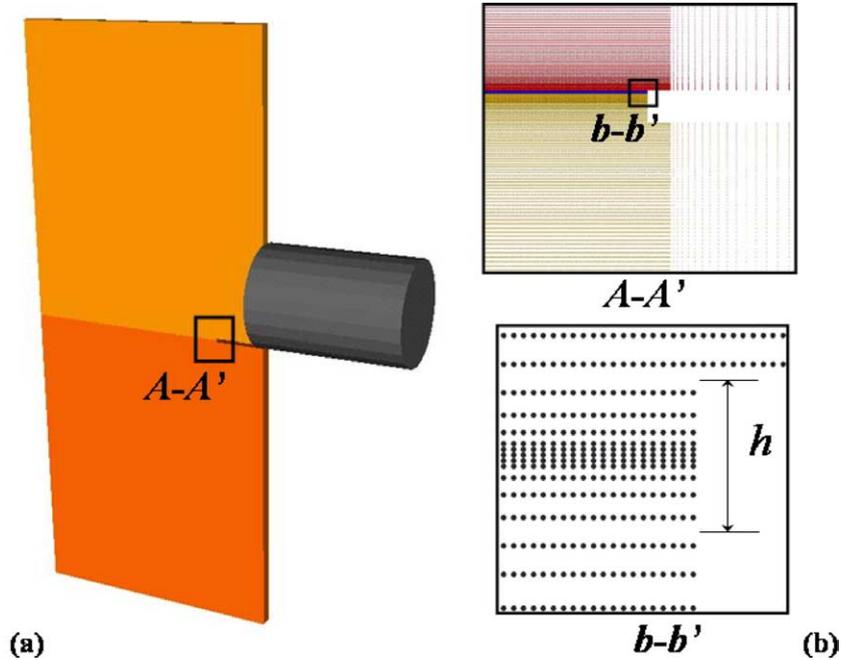
Fig. 5. Particles modeling of the three-phase model introduced in Fig. 2 (the A–A′ image will be removed).

Table 2
Parameters applied in numerical simulations

l (mm) material intrinsic length	h (mm) bonding layer thickness	σ_{Y0} (MPa) bonding strength	m strain rate hardening exponent	V_p (m/s) impact velocity	W_p (mm) distance from the projectile to the notch	F_r friction coefficient (outside fracture process zone)
0.02, 0.04, 0.07, 0.10, 0.20	0.01, 0.02, 0.05, 0.10, 0.16	27, 14, 7	0.01, 0.1	10, 20, 30, 40, 70	0.5, 2.5, 5.5, 9.5, 25	0, 1.0

The numerical study was conducted by varying material intrinsic length, bonding layer thickness, strain rate, bonding strength, loading condition, and impact velocities. The values of these parameters are listed in Table 2.

3.2. Numerical schemes

The moving particle finite element method (MPFEM) (Hao et al., 2002; Hao and Liu, 2002; Hao et al., in press), a new numerical method based on conventional finite element method (Oden, 1972; Hughes, 1987; Belytschko et al., 2000) and the meshfree methodologies introduced in Belytschko et al. (1994) and Liu et al. (1995, 1996, 1997), has been applied in the numerical analysis. The idea of the method can be briefly described using the boundary value problem illustrated in Fig. 6a. An interpolated solution of displacement u in a finite element can be expressed as
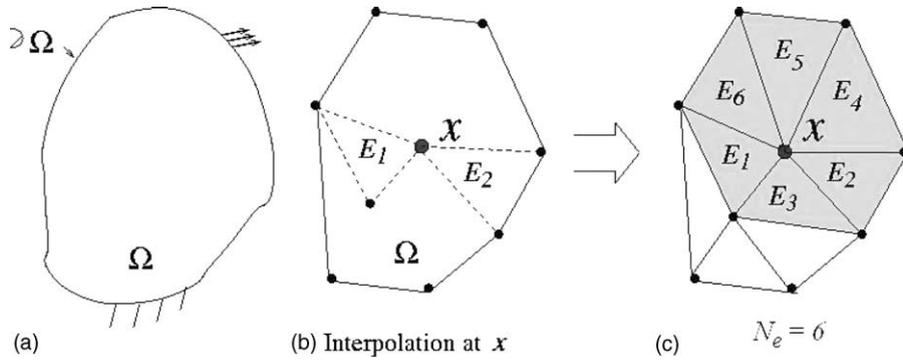
Fig. 6. (a) A boundary value problem defined on $\bar{\Omega}(=\Omega\cup\partial\Omega)$. (b) An approximated solution at x can be obtained from either element E_1 or E_2. (c) MPFEM approximation—an average from the surrounding elements.

$$u(\mathbf{x}) = \sum_{I=1}^{NE} N_I^E(x) \cdot u_I^E$$

where $N_1^E(x)$ is the interpolation function (shape function) for element E, u_I^E is the displacement u at node I in element E, and NE denotes the total number of nodes in element E. The derivative of the field $u(x)$ at a point x (see Fig. 6b) can be obtained either through the interpolation of its left side element E_1 or the right side element E_2:

$$\frac{\mathrm{d}u(\mathbf{x})}{\mathrm{d}x}\bigg|_{E_1} = \sum_{I=1}^{NE_1} \frac{\mathrm{d}N_I^{E_1}(x)}{\mathrm{d}x} u_I^{E_1} \quad \text{or} \quad \frac{\mathrm{d}u(\mathbf{x})}{\mathrm{d}x}\bigg|_{E_2} = \sum_{I=1}^{NE_2} \frac{\mathrm{d}N_I^{E_2}(x)}{\mathrm{d}x} u_I^{E_2}$$

where $N_1^{E_i}(x)$ is the shape function for element E_i, NE_1 and NE_2 represent the number of nodes in elements E_1 and E_2, respectively. For regular finite element method, a gap exists between these two interpolations though they approach a convergent solution when the finite elements become very small. This is because derivatives in conventional finite element solutions are discontinuous at element edges. The concept of the MPFEM can be interpreted as a weighted summation of the solution from all finite elements adjacent to x, as illustrated in Fig. 6c:

$$\frac{\mathrm{d}u(\mathbf{x})}{\mathrm{d}x} = \sum_{i=1}^{N_e} \varpi_i \left\{ \sum_{I=1}^{NE_i} \frac{\mathrm{d}N_I^{E_i}(\mathbf{x})}{\mathrm{d}x} u_I^{E_i} \right\} \tag{6a}$$

where the weight ϖ_i is calculated by minimizing the interpolation error using a meshfree scheme, which removes the numerical discontinuity at element edges. Therefore, the basic idea of MPFEM can be interpreted as an interpolation of finite element interpolation, which combines salient features of finite element and meshfree methods while alleviates certain problems that plague meshfree techniques. It displays considerable stability under large deformations and efficiency with acceptable accuracy, especially for dynamic problems involving high speed impacts. A detailed description of MPFEM can be found in literatures, e.g. in Hao et al. (in press).

For the intersonic crack propagation, the numerical analysis is carried out using a Lagrangian, large deformation Galerkin formulation (Belytschko et al., 2000). The pinball contact algorithm (Belytschko and Neal, 1991) is applied in the simulation. The reviews of the recent developments of meshfree methods can be found in Belytschko et al. (1996) and Babuska et al. (in press).
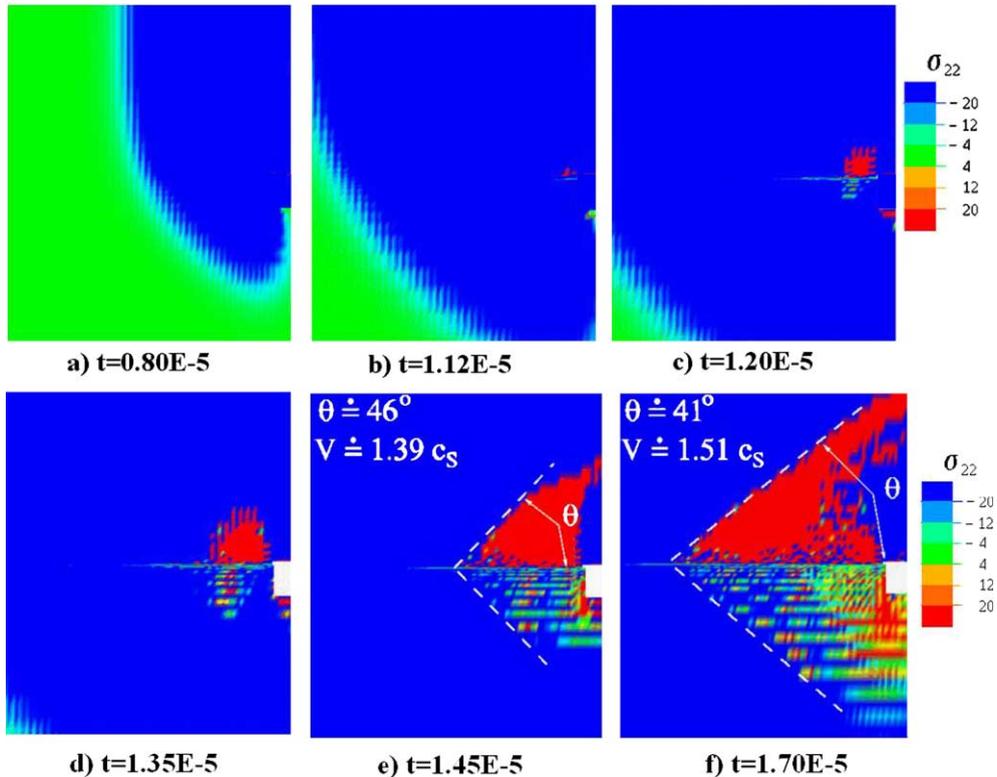
Fig. 7. Fracture process zone initiation and subsequent crack propagation. (a) $t = 0.80e-5$, (b) $t = 1.12e-5$, (c) $t = 1.20e-5$, (d) $t = 1.35e-5$, (e) $t = 1.45e-5$ and (f) $t = 1.70e-5$.

4. Results and discussion

4.1. Crack initiation—an observation

Fig. 7 presents a set of snapshots of the numerical simulation of the specimen shown in Fig. 2. The contours of the stress σ_{22}, which is normal to the crack propagation path, are displayed in the vicinity of the notch tip at different time steps. According to these figures, intersonic crack initiation may be divided into four stages:

1. Initial wave propagation (Fig. 7a and b): the impact of the projectile induces a dilatational wave that (dark blue color) sweeps transversely over the specimen with a distinct wave front. However, two kinds of shear wave impulses could also exist behind the dilatation wave front but they are overshadowed in these figures. They are the impact induced shear wave, which is behind the dilatation wave front with the distance $t(c_l - c_s)$ where t is time, and the reflect shear wave when the dilatation wave impulse hits the traction-free notch surface and bi-material interface.
2. After the dilation wave front has passed, a drop of σ_{22} can be seen along the bonding layer ahead the notch tip (Fig. 7b and c), marked as the line segment with light color emanated from the notch tip. This drop is caused by the nucleation of a fracture process zone after the onset of material decohesion. Within this zone, the softening of the interface material results in the localized fluctuation of stresses.

3. Crack initiation (Fig. 7c and e): After a considerable fracture process zone formed, a significant stress drop occurs in a relatively large area near the notch end, characterized by an increasing stress noise radiation at both sides of the bonding layer, which can be interpreted as a crack initiation that creates nearly traction-free new surfaces. It is well-known that a crack induced by mode II loading is always accompanied by some mode I crack opening, which relaxes the impact induced compressive σ_{22} and results in a shock-like contour of stress noise (red color).

4. Acceleration and steady-state propagation (Fig. 7e and f): the angle between stress shock front and bonding layer becomes smaller, implying that the crack growth is speeding up. In general this angle θ is related to the propagation speed v through the relation (Weertman and Weertman, 1980):

$$\theta = \sin^{-1}\left(\frac{c_s}{v}\right) \tag{7}$$

when $v \geqslant c_s$.

Crack propagation can be considered as the accumulation of damage in the forms of micro-defects (such as voids or micro-cracks) nucleation, growth, and coalescence. This process is characterized by the fast softening stage defined in (4) and (5) of the constitutive model (see Figs. 3 and 4). When the dilatation wave front hit the notch tip, the resulting shear stress causes the softening of the bonding layer material and triggers spontaneous debonding along the weak path, which is reflected as the fracture process zone emanating from the notch tip, as shown in Fig. 7.

Fig. 8 shows a comparison with experimental observations (Rosakis et al., 1999). The simulation results in Fig. 8b show a strain (ε_{22}) shock angle about 44° which is consistent with the experimental measurement (Fig. 8a). As depicted in Fig. 8c, the simulated crack propagation speed, calculated using (7), agrees with experiments.

4.2. Stress wave motion and decohesion

Fig. 9 illustrates an overview of the wave propagation mechanism for the specimen of Fig. 2. The stress distributions along the line AA′ in Fig. 9a are displayed in Fig. 9b at three times, in which the dilatation wave propagation demonstrated in Fig. 7 is actually formed by a rectangular-like σ_{11} impulse, plotted as the dashed line in Fig. 9b. The σ_{11} impulse front, is accompanied simultaneously with the σ_{22} and σ_{12} components. Fig. 9b at time $t = 2.0e-5$ shows the convex-shaped σ_{12} and σ_{22} impulses. This σ_{12} impulse actually imposes a mode II load on the notch tip, which triggers the fracture process zone initiation and drives it to
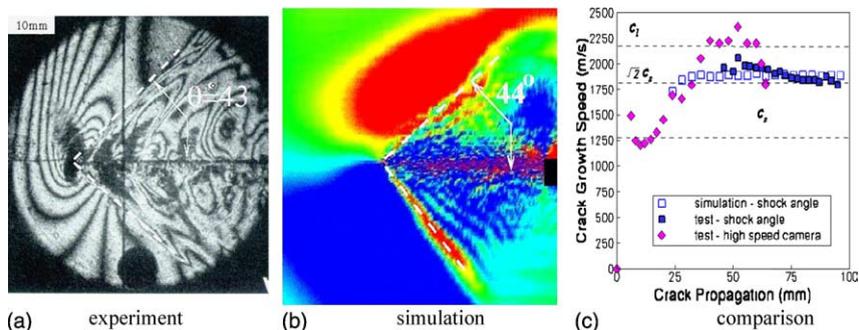
Fig. 8. A comparison between numerical simulation and experiment (Rosakis et al., 1999). (a) Experiment; (b) simulation and (c) comparison.
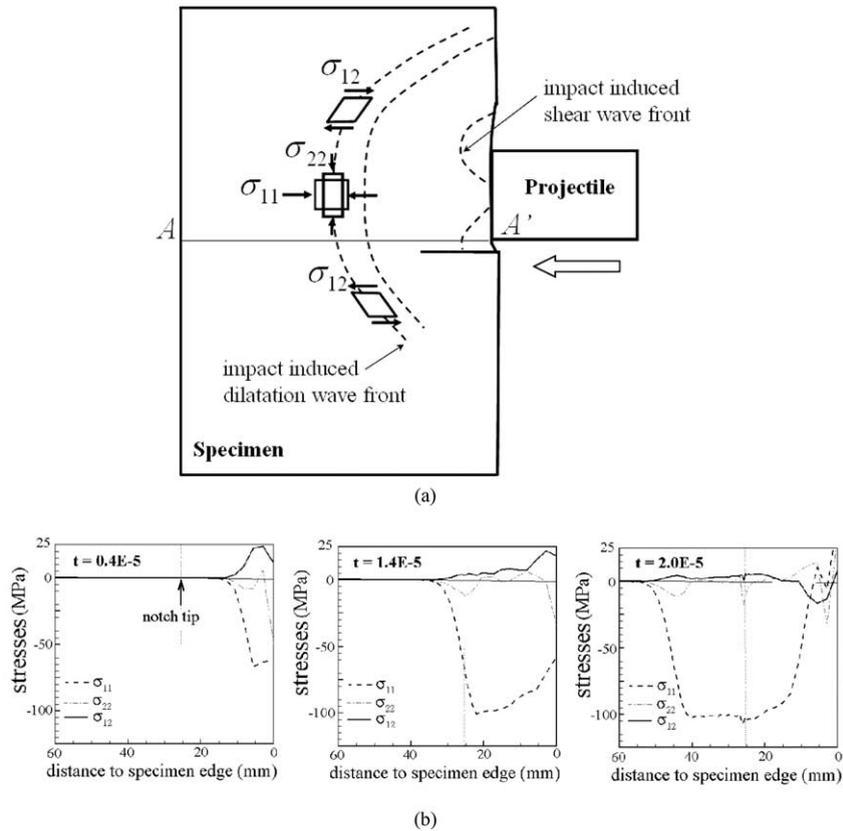
Fig. 9. (a) An illustration of the dilatation wave propagation and the corresponding stress state. (b) Stresses distribution along the line AA' in (a).

move forwards along the weak path. The amplitude of σ_{11} impulse remains nearly constant while both the σ_{22} and σ_{12} decay earlier as new crack surfaces are formed. The trailing random stress impulses are the result of crack face contact and wave reflections.

The numerical results demonstrate that the combination of computation and analysis may provide insight for designing a dynamic fracture specimen. For the specimen shown in Fig. 1, to achieve a mode II-like loading along the weak path requires the maximum shear stress and minimum normal compressive stress σ_{22}, which causes contact, around the notch tip. Considering the dilatation wave front as the envelop of the dilatation waves radiated from the point sources along the contact surface between specimen and projectile, the maximum σ_{12} is attained when the tangent of the envelop declines to the notch with the angle of $\pi/4$. This preliminary analysis estimates that the optimal W_p in Fig. 2 should be the same as the length of the pre-manufactured notch.

4.3. Definition of the "fracture process zone"

A precise definition of the "fracture process zone" is crucial for interpreting the results of a numerical simulation in terms of quantitative analyses. According to the constitutive law defined in (4) and (5–5b), decohesion begins when the equivalent plastic strain reaches $[\bar{\varepsilon}]^{\text{bifurc}}$ that characterizes the onset of material
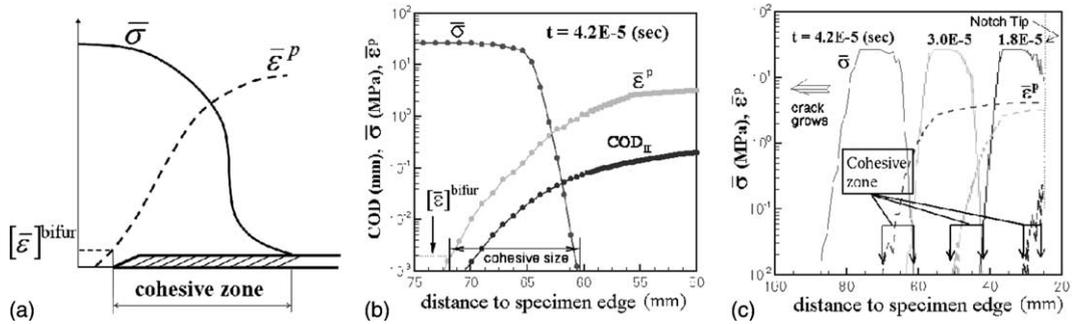
Fig. 10. Definition and measurement of cohesive zone (fracture process zone) in the numerical simulation. (a) Definition; (b) a numerical example; (c) measurement of a moving fracture process zone during crack growth.

bifurcation. This leads to an unambiguous definition (Fig. 10a): the fracture process zone starts where $\bar{\varepsilon}^p = [\bar{\varepsilon}]^{bifur}$ and ends where the stress drops to zero. The physical meaning of the end of a fracture process zone is obvious: when a material suffers enough deformation and thus is fully damaged, it loses the capacity to sustain stress; which results in cracking.

The computed equivalent stress and strain along the bonding layer are plotted in Fig. 10b, illustrating the fracture process zone measurement in this study. The mode II crack opening displacement (COD) is also plotted in this figure, where the COD is defined as the separation between upper and lower boundaries of the bonding layer. A time sequence of the computed equivalent stresses and strains along the bonding layer are displayed in Fig. 10c.

4.4. Contact mechanism and self-healing phenomenon

The numerical simulation demonstrates that contact between newly formed crack surfaces is inevitable during intersonic crack propagation in the specimen shown in Fig. 2 due to the material stretching perpendicular to impact direction. The contact mechanisms for such a dynamic crack growth can be explained through the four deformation regions that are illustrated in Fig. 11a–c. They are: (I) decohesion zone (fracture process zone), (II) opening, even under shear dominant loading, (III) crack closure leading to contact among the material elements within the bonding layer, (IV) contact between two matrices. Stage IV occurs only when the material in the bonding layer is fully damaged thus losing its capacity to sustain any load according to the constitutive law (4) and (5).

Fig. 12 presents snapshots of the contours of equivalent plastic strain, strain gradient, and shear strain within the bonding layer from a computation with $h = 2l$, where the vertical scale has been significantly enlarged while the horizontal scale sustains. In this computation the upper half part of the specimen is hit by a projectile. The equivalent plastic strain and strain gradient are plotted on the undeformed configuration whereas the shear strain contours are plotted on the deformed configuration. The decohesion-induced plastic strain (the contours with red color) represents the crack opening profile that is actually composed of these fully damaged material elements, which are mainly concentrated in the upper half layer with a width close to the material intrinsic length l. However, considerable plastic strain also exists in the rest of the layer. Ultimately, all material elements in the bonding layer are fully damaged in the contact zone IV.

The contact zone II introduced in Fig. 11 represents an opening dominated crack profile that forms even under shear loading. This zone was detected using the results shown in Fig. 13 where the σ_{12} and σ_{22}
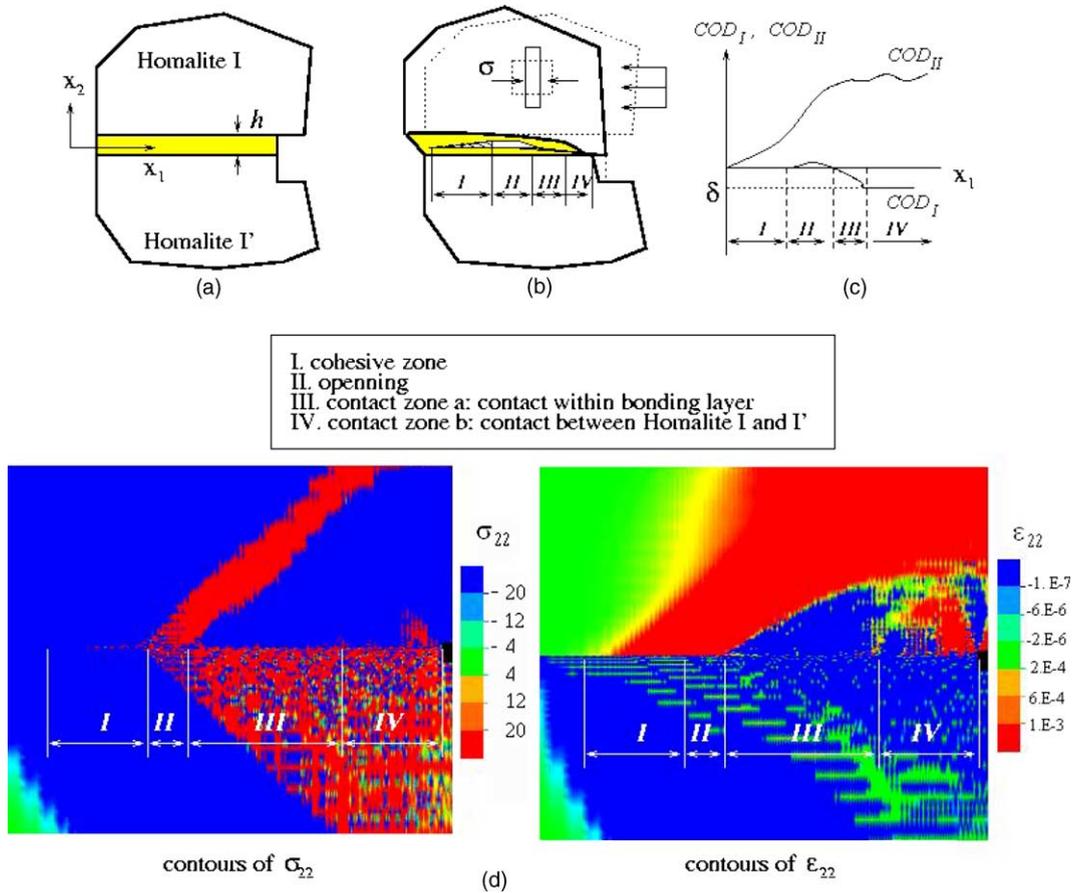
Fig. 11. An illustration of the effects of contact on crack opening closure profile. (a) The structure before impact. (b) After impact: an illustration of deformation induced contact. (c) Crack opening (sliding) profiles. (d) Stress and strain shocks corresponding to crack opening (sliding) and contacts.

are plotted along the bonding layer. Behind the convex peaks caused by impact induced impulse, both stresses nearly vanish until the contact zone III, which is characterized by the fluctuating stress distribution along the bonding layer. The stress shock presented in Fig. 7 is another result of the contact zone II.

Plotted in Fig. 14 are the COD_I^* (mode I COD) and COD_{II}^* (mode II COD) along the crack growing path at three time steps, normalized by h, the bonding layer thickness. These diagrams show that COD_I^* is negative, indicating that the crack faces are driven into contact. However, after a certain amount of crack growth the COD_I^* stays at the constant value about $-h$ while the increase of COD_{II}^* is also slows (Fig. 14c), which hints that the contact between two matrices occurs and the relative sliding between them almost diminishes after the bonding layer material is fully damaged. This phenomenon is quite similar to the self-contact/healing process that has been frequently observed in seismic motion (Perrin et al., 1995; Ben-Zion, 2001).

Theoretically, COD is defined over an idealized crack that is a line without width. In the numerical simulations, it is measured over the gauge length h, denoted by the superscript ∗, which is actually a
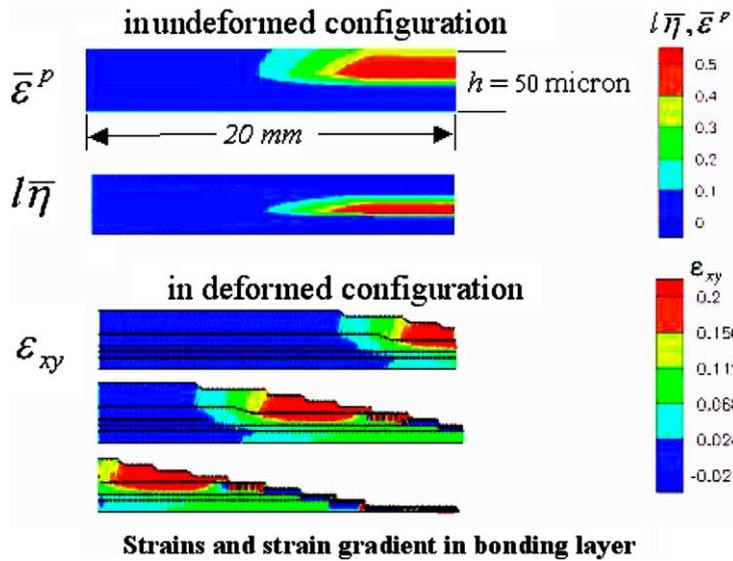
Fig. 12. Contours of plastic strain, strain gradient, and shear strain in the bonding layer.
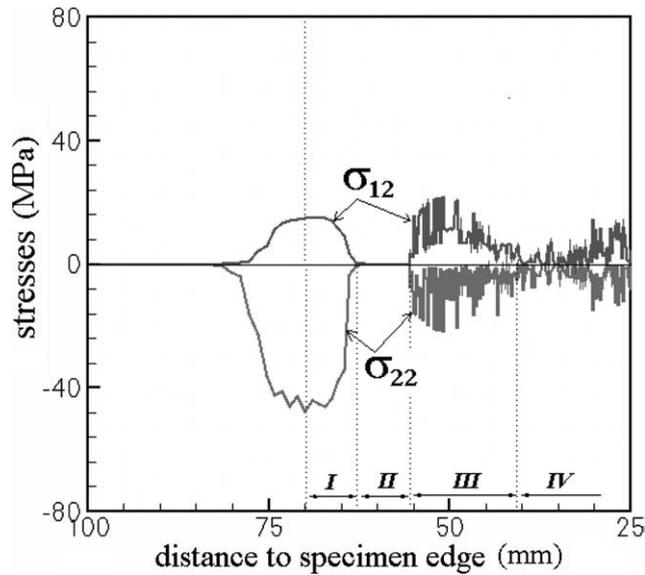
Fig. 13. The shear and normal stresses on a propagating crack surface.

measurement of the average deformation over the bonding layer material. This average overshadows the tiny positive COD_I along the new crack surfaces.

In Fig. 15, the mode II separation is plotted with respect to a moving coordinate system with its origin fixed to the tip of the fracture process zone. Over the different time steps, an almost constant crack opening profile is present, indicating a nearly steady-state propagation.
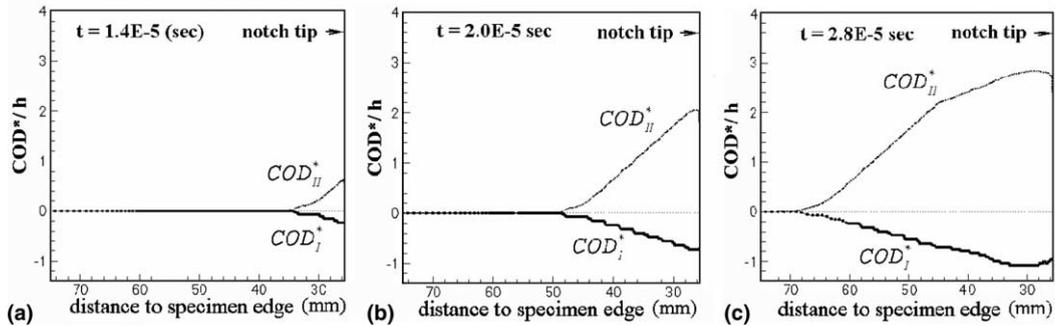
Fig. 14. A numerical example of mode I and II opening profiles during propagation, where h is the thickness of the bonding layer; in (c) the I, II, III, IV refer to the contact zones illustrated in Fig. 11.
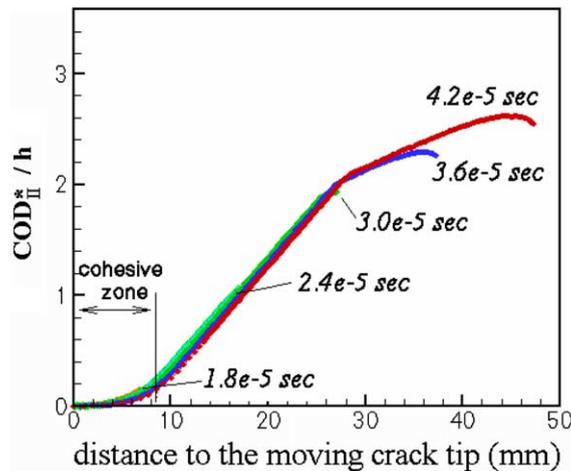
Fig. 15. The mode II crack opening profiles during propagation, plotted in a coordinate frame fixed to the moving crack tip.

4.5. The effects of length scales: a parameter study

Dual functions have been assigned to the material intrinsic length l in the constitutive equations (4) and (5): governing the strain gradient induced hardening before material bifurcation and scaling the energy dissipation in post-bifurcation stage (see Figs. 3 and 4). Comparing Fig. 3 with Fig. 10 that illustrates the definition of fracture process zone, one can find that the intrinsic length l actually scales the size of fracture process zone and the decohesion energy.

The crack tip in the specimen in Fig. 2 is governed by the elastic–plastic field within the bonding layer and the elastic field in the surrounding matrices. The material extrinsic length, the thickness h, determines the ratio of the influences from these two fields on the crack tip. The slip-field analysis in Hao et al. (1997) reveals that h also determines the amplitude of the stress triaxiality in the bonding layer.

These functions of l, h and their effects on intersonic growth are studied quantitatively in this subsection.

According to dislocation theory (Weertman and Weertman, 1980) the decohesion energy within the fracture process zone can be calculated by:

$$G_R = -\frac{1}{2} \int_{\Delta a_C} D(X_1)\sigma_{12}(X_1)\,\mathrm{d}X_1 \tag{8}$$

where the coordinate X_1 is originated at the crack tip and Δa_C represents the length of fracture process zone; $D(X_1)$ is related to the mode II separation by:

$$D(X_1) = -2[u_1]_{,1} \tag{9}$$

Eq. (8) can also be derived by calculating the J-integral along a contour surrounding the fracture process zone along the lower and upper boundaries of the bonding layer.

Fig. 16 shows the evolution of decohesion energy G_R computed using (8) with crack length a and time t, respectively, with varying l. Two stages can be identified in both $G_R(a)$ and $G_R(t)$ curves: crack initiation-acceleration stage and steady-state propagation. Initially, G_R increases while the slopes $\frac{\mathrm{d}G_R}{\mathrm{d}a}$ and $\left(\frac{\mathrm{d}G_R}{\mathrm{d}t}\right)$ decrease with increasing a and t. Both $G_R(a)$ and $G_R(t)$ finally approach constant levels whereas the average value of $\frac{\mathrm{d}G_R}{\mathrm{d}a}$ or $\left(\frac{\mathrm{d}G_R}{\mathrm{d}t}\right)$ approaches zero, implying a steady-state propagation. The amplitude of G_R is nearly linearly proportional to the material intrinsic length l in this stage.

Plotted in Fig. 17 are the fracture process zone sizes against time and crack length, respectively. They demonstrate a similar trend as those shown in Fig. 16. These numerical results demonstrate that at steady-state propagation stage, the fracture process zone size Δa_C attains a size that is linearly proportional to material intrinsic length, i.e.

$$\Delta a_C = l \cdot F(\text{material constants}, h) \tag{10}$$

where F is a function of material constants and extrinsic length h. According to Fig. 3, l scales energy dissipation at softening stage. For a linear softening, l actually is the inverse of w, the slope of the traction-separation law; thus

$$\Delta a_C \propto \frac{F(\text{material constants}, h)}{w} \tag{11}$$

(10) or (11) conforms the general conclusion that is obtained by the theoretical analysis of Uenishi and Rice (2003).
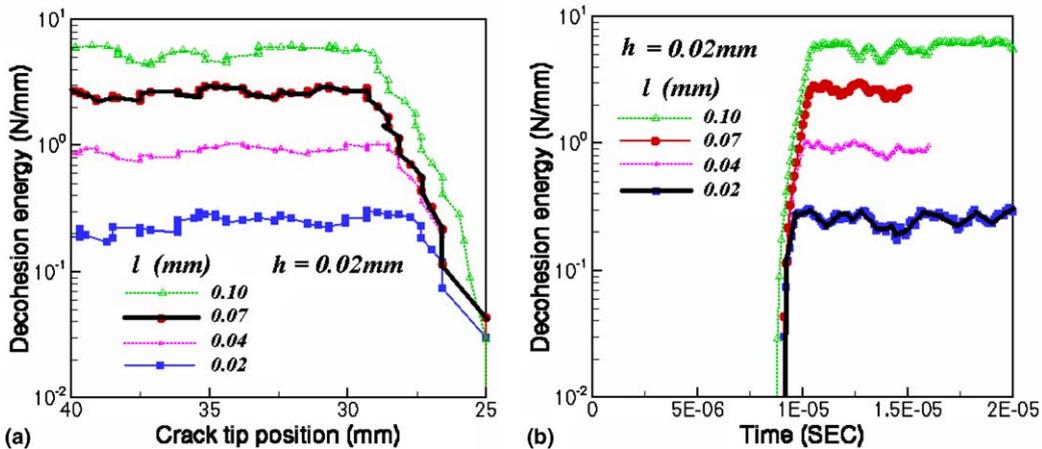
Fig. 16. The effect of material intrinsic length on the decohesion energy. (a) Decohesion energy vs. crack tip position and (b) decohesion energy vs. time.
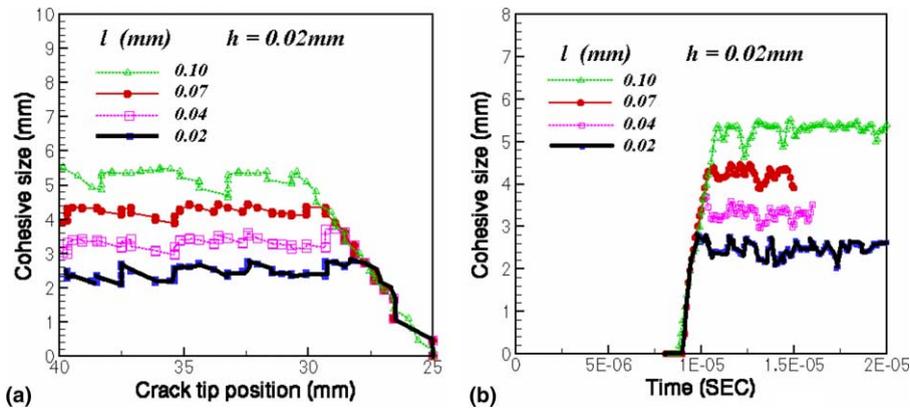
Fig. 17. The effect of material intrinsic length on fracture process zone size. (a) Process zone size vs. crack tip position and (b) process zone size vs. time.
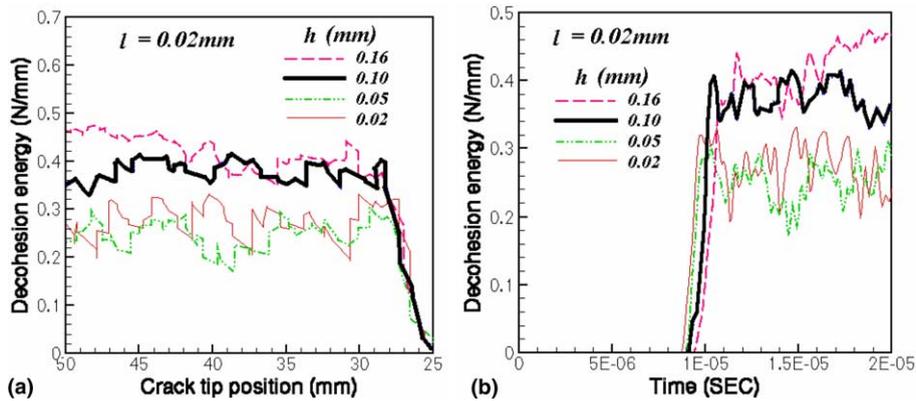
Fig. 18. The effect of bonding layer thickness on decohesion energy. (a) Decohesion energy vs. crack tip position and (b) decohesion energy vs. time.

Presented in Figs. 18 and 19 are another set of simulations with fixed l but varying h, demonstrating that smaller h also results in less energy dissipation and shorter fracture process zone. The slip-field analysis from Hao et al. (1997) indicates that a smaller ratio of h to the specimen thickness produces higher stress triaxiality and strain gradient within the bonding layer, which drives damage evolution and accelerates failure of the bonding layer material. Consequently, it accelerates decohesion and debonding. On the other hand, smaller h reduces the contribution of the elastic plastic stress–strain field in the bonding layer because there is less space left for such a kind of deformation. All of these make the bonding layer more ''brittle'', represented by less energy dissipation and shorter fracture process zone size.

4.6. Crack propagation speed

4.6.1. Intersonic and supersonic propagation

We define the propagation speed of the leading edge of fracture process zone as the crack speed. Fig. 20a shows the variation in propagation speed with crack tip position from two computations with the same length scales ($l = 0.02$, $h = 0.02$) but different strain rate hardening power m, as defined in (5). Similar to
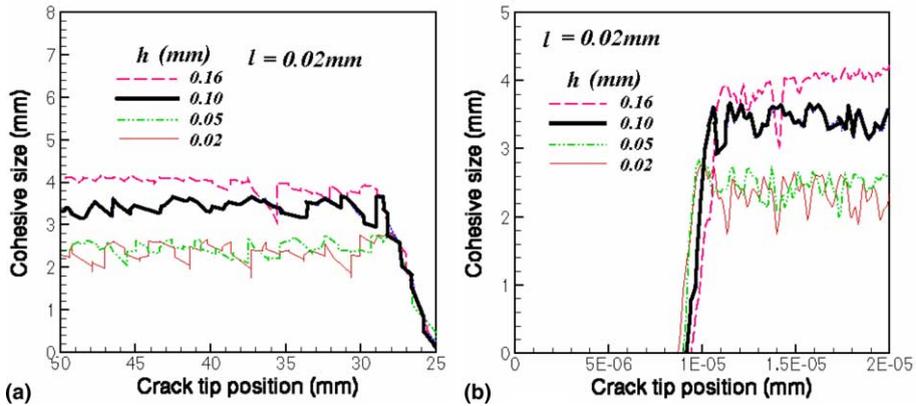
Fig. 19. The effect of bonding layer thickness on cohesive size. (a) Cohesive size vs. crack tip position and (b) cohesive size vs. time.

the results illustrated in Fig. 7, the propagation speed for both cases accelerates to the supersonic regime in a very short time when the fracture process zone bursts out from the notch tip. Then it falls back into the intersonic regime, followed by propagation at speeds fluctuating between c_l and $\kappa_0 c_s$, where κ_0 is about $\sqrt{2}$ for the case $m = 0.01$ and 1 for the case $m = 0.1$. The spacing of each oscillation is about 1.5–2 mm of crack growth. The average speeds, which can be determined as the average slope of the $a(t)$ curve, lie in the region between $\sqrt{2}c_s$ and c_l for both cases.

Fig. 20b and c show the corresponding stress shocks. For the case with a larger m (Fig. 20c), two stress shocks appear in the lower half of the specimen. The first arc-shaped stress shock characterizes supersonic-like propagation as it appears only when the propagation speed surpasses the dilatational wave speed. The second shock appears when propagation is faster than shear stress wave. This observation supports the results shown in Fig. 20a where the average propagation speed for this case is close to the dilatational wave speed and the upper bound of the propagation speed surpasses c_l.

It should be emphasized that all the numerical simulations in the present work show that the fracture process zone, thus crack tip, is always behind the dilatational wave front, e.g. Fig. 7. However, a spontaneous failure along a thin bonding layer occurs after a dilatational wave front sweeps passed, which can
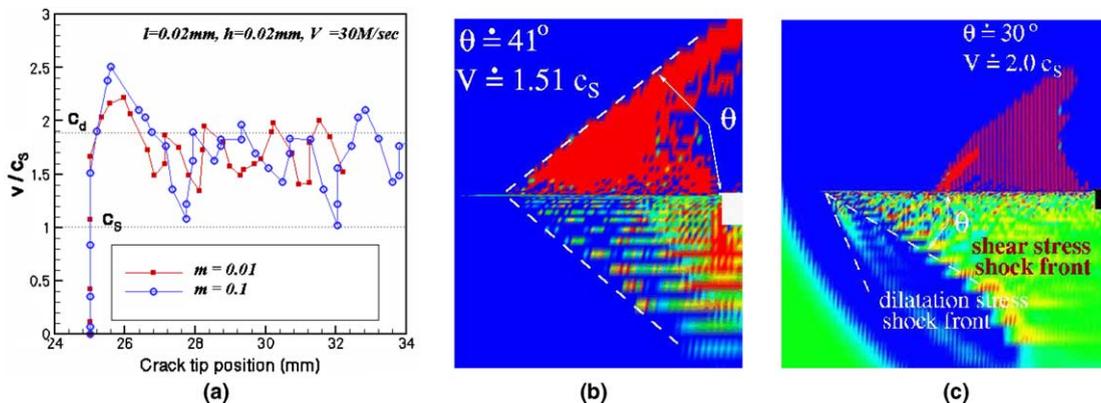
Fig. 20. Intersonic and supersonic crack propagations. (a) Speed vs. crack growth for two simulations with different strain rate hardening power. (b) The stress shock for case with $m = 0.01$. (c) The stress shock for case with $m = 0.1$.

causes the crack front to jump ahead in an instant at faster than c_1. As crack propagation is a non-inertia motion (Freund, 1990), the fracture process zone and crack tip can never surpass the dilatational wave front if there is no previously imposed stress or strain on the weak path. Hence, a supersonic-like weak-path propagation can not be sustained. It will fall back to intersonic regime immediately, as demonstrated in Fig. 20a.

The results presented in Fig. 20 demonstrate that the strain rate hardening power m has strong effects on intersonic crack propagation. A quantitative explanation is that higher strain rate sensitivity (higher m) results in less ductility for the bonding layer material because its yield strength will be elevated and the corresponding softening/damage evolution will be speeded up in the post-bifurcation stage. These results agree qualitatively with the analysis of single dislocation motion in Rosakis (2001).

4.6.2. The effect of remote boundary condition

The simulations with various projectile velocities (V_p) have been performed with other parameters held fixed. The relation between the average crack propagation speed and V_p is plotted in Fig. 21a, which demonstrates a slight elevation of propagation speed when V_p varies from 25 to 70 m/s. Plotted in Fig. 21b are the evolution of decohesion energy against time for the cases in Fig. 21a, from which one can distinguish that higher V_p results in earlier crack initiation.

The diffraction solution of an impact induced stress wave around a crack tip (Achenbach, 1973) indicates that the amplitude of shear stress at the crack tip can be estimated by

$$\sigma_{12} \propto \sqrt{t} \quad \text{and} \quad \sigma_{12}^{max} \cong \frac{E \cdot V_p}{c_1} \tag{12}$$

Hence, at a given instant t, a higher impact speed V_p causes higher stress. The sequence of crack propagation demonstrated in Fig. 21b hints that an intersonic crack initiates when the impact induced shear stress impulse reaches a certain threshold value at the crack tip. Taking the second equation of (12) as the driving force and $\tau_{Y0}(=\frac{\sigma_{Y0}}{\sqrt{3}})$, the shear yield strength of bonding layer, as the resistance, we define a parameter R_s, the ratio of this driving force and resistance:

$$R_s = \frac{\sigma_{12}^{max}}{\tau_{Y0}} = \frac{E \cdot V_p c_1^{-1}}{\tau_{Y0}} \tag{13}$$

to characterize intersonic crack growth. When R_s is greater than R_s^{cr}, the threshold of R_s, intersonic propagation will occur; otherwise, the imposed stress impulse is not strong enough to trigger "spontaneous" debonding along a weak path, and a crack will grow at subsonic speeds. In the cohesive element analysis of Needleman (1999), the bonding strength is taken as a control parameter and a transition from
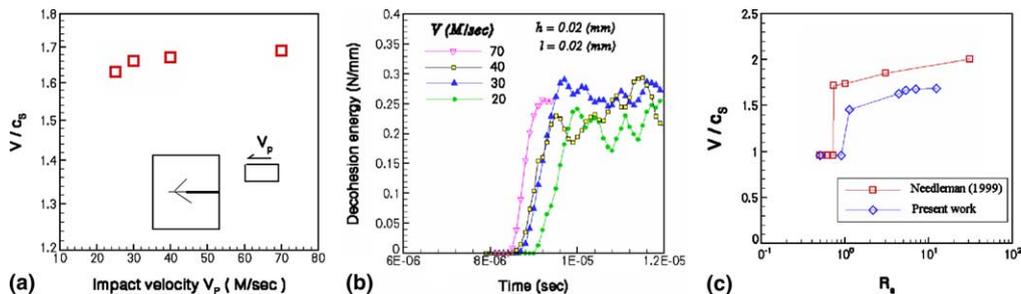
Fig. 21. The effects of strain rate hardening and impact velocity on propagation velocities. (a) The average propagation speed vs. impact velocity. (b) The decohesion energy vs. time for the cases in (a). (c) Nominal crack speed vs. R_s defined in (13).

subsonic to intersonic propagation has been observed when the bonding strength is decreasing. By combining the numerical results in Needleman (1999) with the present work, Fig. 21c presents the relationship between propagation speeds and R_s. This figure shows that the threshold R_s^{cr} is around one.

4.6.3. Comparison with theoretical analysis

A further question is how fast can a crack grow when $R_s > R_s^{cr}$?

Based on the Weertman's moving dislocation solution (Weertman, 1969; Weertman and Weertman, 1980) and Rice–Thomson's dislocation emission model (Rice and Thomson, 1974), a generalized Bilby–Conttrell–Swinden–Dugdale model (Bilby et al., 1963) has been proposed in Hao et al. (in press) (see Fig. 22). In this work, the solutions of steady-state weak-path intersonic crack growth with three classes of cohesive laws have been obtained. In this model the remote boundary condition has been represented as equivalent traction acting on the crack surface, which is expressed as the summation of a constant remote imposed stress τ^{remote} and a non-constant term $\bar{\tau}_d^{remote} D(x)$. The latter can be a remote, imposed stress rate or non-uniform, distributed, remote stress. In this product, the $D(x)$ is given by (9) and $\bar{\tau}_d^{remote}$ is proportional to R_s:

$$\bar{\tau}_d^{remote} = \begin{cases} 0 & \text{for } v \leqslant c_s \\ EQ\left(\frac{R_s}{R_s^{cr}} - 1\right) & \text{for } v > c_s \end{cases} \tag{14}$$

where Q is a function of the specimen geometry which can be calculated through an energy balance.

According the solutions in Hao et al. (in press) the relationships between propagation speed and $\bar{\tau}_d^{remote}$ are plotted in Fig. 23a for different h/l. In this figure each curve includes two parts separated by the saddle point defined by $\kappa_v c_s$, where $\sqrt{2} < \kappa_v \leqslant c_l/c_s$. In the interval $c_s < v < \kappa_v c_s$ crack growth is unstable as the propagation speed will be increasing while $\bar{\tau}_d^{remote}$ decreases. The interval $\kappa_v c_s \leqslant v < c_l$ represents a stable propagation regime, in which crack acceleration requires increasing $\bar{\tau}_d^{remote}$. The coefficient κ_v is a function of the material intrinsic and extrinsic lengths, strain rate hardening parameters, and remote boundary condition represented by $\bar{\tau}_d^{remote}$. A comparison between numerical computation and theoretical prediction is given in Fig. 23b. The difference in the results is due to the slight difference in boundary condition between two approaches.
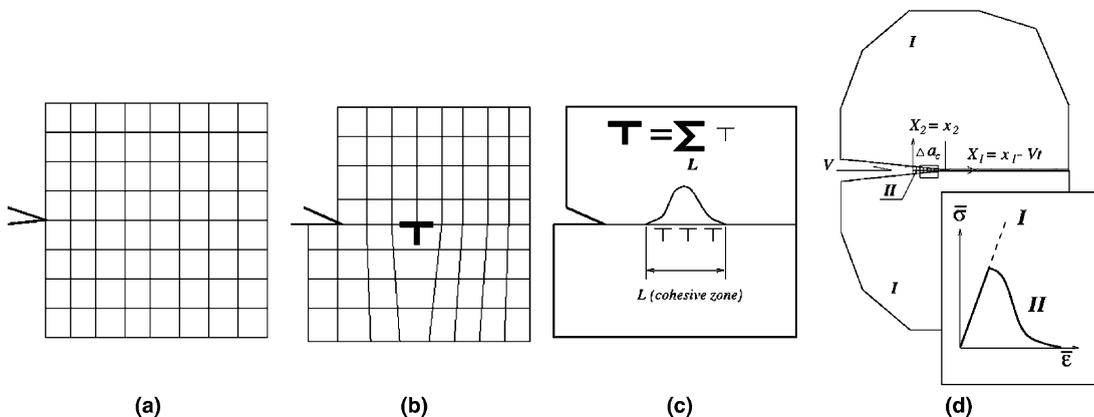
Fig. 22. Dislocation accumulation-induced intersonic crack growth model (Hao et al., in press); (a) lattices before crack growth; (b) dislocation emission (Rice and Thomson, 1974); (c) smeared-out moving dislocation (Weertman's solution, 1969); (d) dislocations accumulation-induced steady-state intersonic crack growth with fracture process zone.
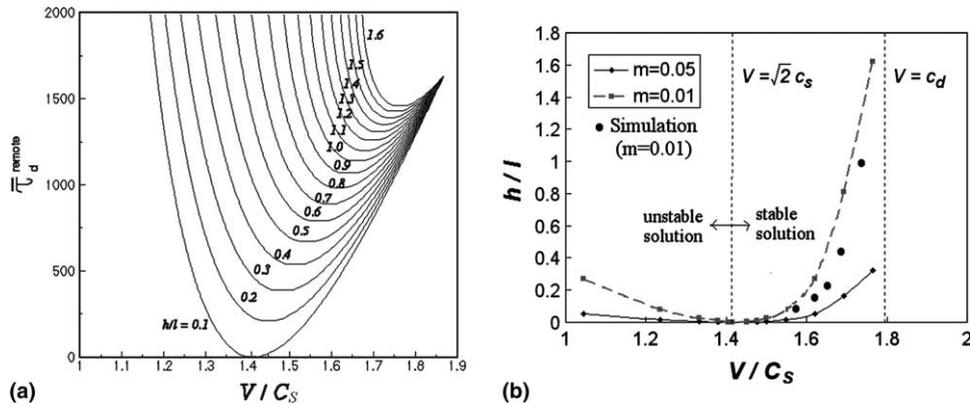
Fig. 23. (a) Relationship between propagation speed V and $\bar{\tau}_d^{\mathrm{remote}}$, theoretical solution (Hao et al., in press); (b) comparison between predictions and present numerical solutions.
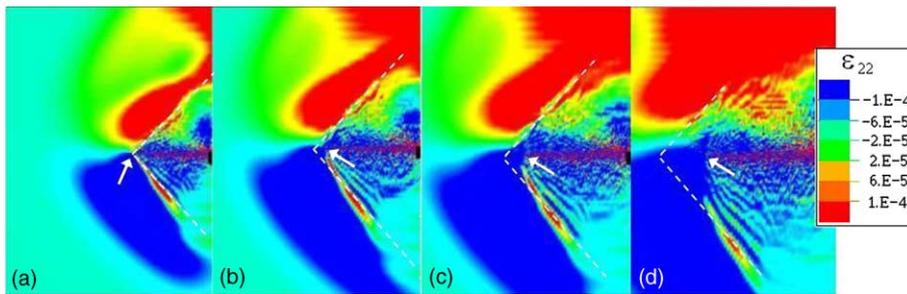
Fig. 24. Intersonic crack propagation deceleration—contours of the strain perpendicular to the crack path where the white arrow indicates the crack tip position in each figure. (a) $t = 1.4\mathrm{e}{-5}$ (s), (b) $t = 1.6\mathrm{e}{-5}$ (s), (c) $t = 1.7\mathrm{e}{-5}$ (s) and (d) $t = 1.95\mathrm{e}{-5}$ (s).

4.7. Sudden deceleration of intersonic crack growth

Two issues are discussed in this subsection: the condition that causes sudden deceleration and the corresponding wave propagation mechanism.

Fig. 24 is a set of the snapshots of strain shocks during a deceleration process, where the white arrow indicates the position of the crack tip in each figure. It demonstrates that before deceleration the crack grows with an intersonic speed, accompanied by a strain shock radiated from the crack tip (Fig. 24a). According to the angle between the strain shock and fracture path, the average propagation speed is about $1.46c_s$. This crack tip shock radiation ceases in Fig. 24b while the existing strain shocks continuously spread out and march forwards passing the moving crack tip (Fig. 24c and d), which implies that the crack propagation has already decelerated to sub-Rayleigh regime.

Fig. 9b indicates that after the projectile impacts the specimen edge, a σ_{11} impulse travels with the dilatational wave speed transversely through the specimen. The shear stress component caused by this dilatational stress impulse triggers the mode II crack initiation and drives it at intersonic speeds when R_s (13) is greater than its threshold R_s^{cr}. Since the average crack propagation speed is always slower than dilatational speed, after the dilatational stress impulse passes the crack tip, R_s drops below R_s^{cr} immediately, so the crack loses its driving force and its propagation speed decreases.
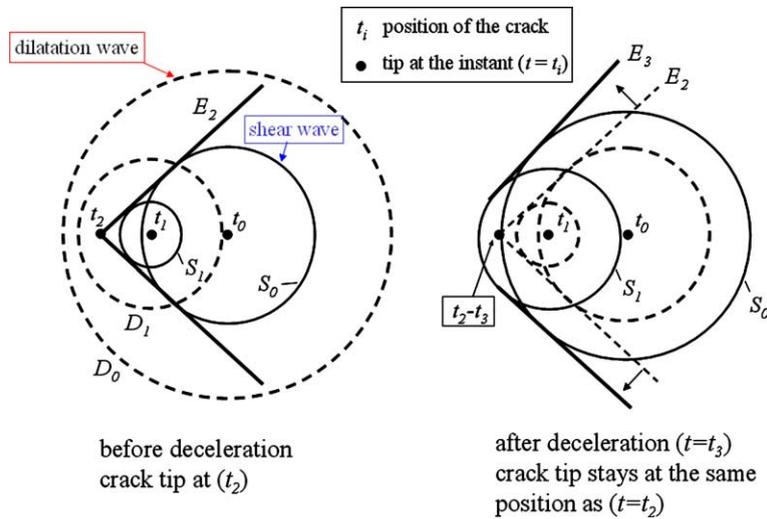
Fig. 25. Wave mechanisms before and after a crack decelerates from intersonic to subsonic speeds where t_i denotes the time, D_i and S_i are the dilatational wave and shear wave radiated from the crack tip at t_i, respectively, and E_i is the envelop of all shear wave fronts at t_i.

Fig. 24 also demonstrates that after crack deceleration, the strain shocks radiated out before deceleration continue to move forward with a constant angle. Several strain shocks appear and one follows another, reflecting the fluctuating propagation speed shown in Fig. 20a. In Fig. 24 the white dash lines indicate the extension of the strain shock fronts. The intersections between these white dash lines and the weak path indicate the position of crack tip if there were no deceleration. It should also be noticed that the strain shocks, which were straight lines before the crack decelerates, become curved bending toward the crack tip. If we consider a moving crack tip as a source which radiates both dilatation and shear waves, the shocks demonstrated in Fig. 24 are actually the envelopes of the shear waves radiated from the crack tip at each instance. When the crack propagation speed decelerates from intersonic regime to subsonic regime, this envelop will degenerate to a curve, as depicted in Fig. 25. It implies that the intersonic steady-state crack tip stress–strain field radiates out from the position where deceleration occurs with a shear wave speed. This phenomenon is similar to the theoretical prediction in Freund's subsonic non-uniform crack motion solution (Freund, 1972) where the equilibrium solution immediately radiates out from the crack tip at a speed less than dilatation wave speed when a sub-Rayleigh crack propagation is suddenly stopped.

5. Conclusions

Intersonic crack growth has been investigated based on the dynamic fracture test conducted by Rosakis and his co-authors (Rosakis et al., 1999). A three-phase interfacial fracture model is proposed for numerical simulations, in which an additional material phase is introduced to reproduce the mechanical behavior of the interface. Numerical simulations have been performed with varying load, material intrinsic and extrinsic length, strain rate hardening exponents. The results and conclusions are summarized as follows:

1. The numerical simulations demonstrate that the crack propagation speed exhibits oscillations ranging from intersonic to supersonic speeds. The upper bound of this oscillation is around the dilatational wave speed whereas the lower bound is around the shear wave speed to $\sqrt{2}$ times shear wave speed, depending

on the material intrinsic length, bonding layer thickness, strain rate sensitivity, and loading conditions. The steady-state propagation speed is the average of these upper and lower limits which lies between $c_s \kappa_v$ and dilatation wave speed, where $\sqrt{2} \leqslant \kappa_v < c_l/c_s$. Both the numerical solution and the theoretical solution, derived from the generalized Bilby–Cottrell–Swinden–Dugdale model (Hao et al., in press), indicate that the coefficient κ_v is a function of the material intrinsic and extrinsic lengths, strain rate hardening parameters, and remote boundary conditions.

2. The parameter R_s, defined as the ratio between remote impact velocity and material shear strength:

$$R_s = \frac{E \cdot V_p}{\tau_{Y0} c_l}$$

is proposed to characterize crack propagation speed. An estimated threshold of R_s defining the boundary between subsonic and intersonic propagation is about unity. When R_s is smaller than its threshold, a crack grows with sub-Rayleigh speed; otherwise, it grows with an intersonic speed.

3. Stress shocks, characterized by both the intersonic and supersonic speeds, have been captured in the numerical simulations for the case where the average crack propagation speed is close to c_l.

4. Two types of contact exist, contact within fracture process zone and contact between the crack wedges behind moving crack tip. In the present simulation the former is taken into account by the constitutive modeling of the interface material phase; the latter is simulated by additional numerical contact algorithm. The contact behind crack tip can cause additional strain shocks. A "self-healing" mechanism, crack surfaces sticking together, has been captured in the simulation. Both material intrinsic and extrinsic lengths have strong effects on the contact behavior.

5. The dual functions of material intrinsic length are presented in the simulations: governing the strain gradient induced hardening before material bifurcation and scaling the dissipated energy after bifurcation. A nearly linear relationship between fracture process zone size and material intrinsic length has been found during steady-state propagation.

6. The material extrinsic length, defined as the bonding layer thickness, determines the ratio of the effects from the elastic–plastic crack tip field inside a bonding layer and the elastic field in the surround matrices. It has a strong effect on the contact/self-healing behind moving crack tip.

7. Crack deceleration from intersonic to subsonic speeds has been also captured in the numerical simulations. Crack deceleration occurs after an impact induced dilatational stress impulse passes the crack tip which moves at intersonic speeds. The intersonic stress–strain field, which is characterized by shear stress shock radiation, continuously spreads out at the shear wave speed from the site where deceleration occurs. This observation is similar to the Freund's subsonic non-uniform crack motion solution subjected to general load (Freund, 1972).

Acknowledgements

References

Achenbach, J.D., 1973. Wave Propagation in Elastic Solids. North-Holland Publishing Co, Amsterdam, London.
Andrews, D.J., 1976. Rupture velocity of plane strain shear cracks. Journal of Geophysical Research 81 (32), 5679–5687.

Babuska, I., Banerjee, U., et al., in press. Survey of meshless and generalized finite element methods: a unified approach. Acta Numerica.

Belytschko, T., Neal, M.O., 1991. Contact–impact by the pinball algorithm with penalty and Lagrangian-methods. International Journal for Numerical Methods in Engineering 31 (3), 547–572.

Belytschko, T., Lu, Y.Y., Gu, L., 1994. Element-free Galerkin methods. International Journal for Numerical Methods in Engineering 37, 229–256.

Belytschko, T., Krongauz, Y., Organ, D., Fleming, M., Krysl, P., 1996. Meshless methods: an overview and recent developments. Computer Methods in Applied Mechanics and Engineering 139 (1–4), 3–47.

Belytschko, T., Liu, W.K., Moran, B., 2000. Nonlinear Finite Elements for Continua and Structures. John Wiley & Sons, New York.

Ben-Zion, Y., 2001. Dynamic ruptures in recent models of earthquake faults. Journal of the Mechanics and Physics of Solids 49 (9), 2209–2244.

Bilby, B.A., Cottrell, A.H., Swinden, K.H., 1963. The spread of plastic yield from a notch. Proceedings of the Physical Society (London) A 272, 304–314.

Bouchon, M., Bouin, M.P., Karabulut, H., Toksoz, M.N., Dietrich, M., Rosakis, A.J., 2001. How fast is rupture during an earthquake? New insights from the 1999 Turkey earthquakes. Geophysical Research Letters 28 (14), 2723–2726.

Broberg, K.B., 1999a. Cracks and Fracture. Academic Press, London.

Broberg, K.B., 1999b. Intersonic crack propagation in an orthotropic material. International Journal of Fracture 99 (1–2), 1–11.

Burridge, R., Conn, G., et al., 1979. Stability of a rapid mode-II shear crack with finite cohesive traction. Journal of Geophysical Research 84 (NB5), 2210–2222.

Dmowska, R., Rice, J.R., 1986. Fracture theory and its seismological application. In: Continuum Theories in Solid Earth Physics. Elsevier.

Dwivedi, S.K., Espinosa, H.D., submitted for publication. Modeling dynamic crack propagation in fiber reinforced composite including frictional effects. Mechanics of Materials (special issue) honoring Sia Nemat-Nasser.

Federici, L., Nobile, L., Piva, A., Viola, E., 2001. On the intersonic crack propagation in an orthotropic medium. International Journal of Fracture 112 (1), 69–85.

Freund, L.B., 1972. Crack propagation in an elastic solid subjected to general loading. Journal of the Mechanics and Physics of Solids 20, 141–152.

Freund, L.B., 1979. Mechanics of dynamic shear crack-propagation. Journal of Geophysical Research 84 (NB5), 2199–2209.

Freund, L.B., 1990. Dynamic Fracture Mechanics. Cambridge University Press, Cambridge.

Gao, H.J., Huang, Y., Nix, W.D., Hutchinson, J.W., 1999. Mechanism-based strain gradient plasticity—I. Theory. Journal of Mechanics and Physics of Solids 47, 1239–1263.

Gao, H.J., Huang, Y.G., Abraham, F.F., 2001. Continuum and atomistic studies of intersonic crack propagation. Journal of the Mechanics and Physics of Solids 49 (9), 2113–2132.

Geubelle, P.H., Kubair, D.V., 2001. Intersonic crack propagation in homogeneous media under shear-dominated loading: numerical analysis. Journal of the Mechanics and Physics of Solids 49 (3), 571–587.

Gumbsch, P., Gao, H., 1999. Dislocations faster than the speed of sound. Science 283 (5404), 965–968.

Guo, G.F., Yang, W., Huang, Y., Rosakis, A.J., 2003. Sudden deceleration or acceleration of an intersonic shear crack. Journal of the Mechanics and Physics of Solids 51 (2), 311–331.

Hao, S., Liu, W.K., 2002. Moving particle finite element method with global superconvergence. In: The 5th World Congress on Computational Mechanics, Vienna, Austria.

Hao, S., Cornec, A., Schwalbe, K.-H., 1997. Plastic stress–strain fields and limit loads of a plane strain cracked tensile panel with a mismatched welded joint. International Journal of Solids and Structures 34 (3), 297–316.

Hao, S., Liu, W.K., Chang, C.T., 2000a. Computer implementation of damage models by finite element and meshfree methods. Computer Methods in Applied Mechanics and Engineering 187 (3–4), 401–440.

Hao, S., Liu, W.K., Dong, Q., 2000b. Localization-induced band and cohesive model. Journal of Applied Mechanics—Transactions of the ASME 67 (4), 803–812.

Hao, S., Liu, W.K., Klein, P., 2000c. Multi-scale damage model, Chicago, IL, USA, IUTAM 2000.

Hao, S., Park, H.S., Liu, W.K., 2002. Moving particle finite element method. International Journal for Numerical Methods in Engineering 53 (8), 1937–1958.

Hao, S., Liu, W.K., Weertman, J., in press. Cohesive solutions of intersonic moving dislocation. Philosophical Magazine, A.

Hao, S., Liu, W.K., Belytschko, T., in press. Moving particle finite element method with global smoothness. International Journal for Numercial Methods in Engineering.

Hao, S., Liu, W.K., Moran, B., Vernerey, F., Olson, G.B., in press. Multi-scale constitutive model and computational framework for the design of ultra-high strength, high toughness steels. Computer Method in Applied Mechanics and Engineering.

Hao, S., Moran, B., Liu, W.K., Olson, G.B., in preparation. A hierarchical multi-physics model for design of high toughness steels.

Huang, Y., Wang, W., Liu, C., Rosakis, A.J., 1998. Intersonic crack growth in bimaterial interfaces: an investigation of crack face contact. Journal of the Mechanics and Physics of Solids 46 (11), 2233–2259.

Huang, Y., Wang, W., Liu, C., Rosakis, A.J., 1999. Analysis of intersonic crack growth in unidirectional fiber-reinforced composites. Journal of the Mechanics and Physics of Solids 47 (9), 1893–1916.

Hughes, T.J.R., 1987. The Finite Element Method. Prentice-Hall, New Jersey.

Klein, P., Gao, H.J., 1998. Crack nucleation and growth as strain localization in a virtual-bond continuum. Engineering Fracture Mechanics 61, 21–48.

Liu, W.K., Jun, S., Zhang, Y.F., 1995. Reproducing kernel particle methods. International Journal for Numerical Methods in Fluids 20, 1081–1106.

Liu, W.K., Chen, Y., Chang, C.T., Belytschko, T., 1996. Advances in multiple scale kernel particle methods. Computational Mechanics 18 (2), 73–111.

Liu, W.K., Li, S.F., et al., 1997. Moving least-square reproducing kernel methods. 1. Methodology and convergence. Computer Methods in Applied Mechanics and Engineering 143 (1–2), 113–154.

Needleman, A., 1999. An analysis of intersonic crack growth under shear loading. Journal of Applied Mechanics—Transactions of the ASME 66 (4), 847–857.

Needleman, A., Rosakis, A.J., 1999. The effect of bond strength and loading rate on the conditions governing the attainment of intersonic crack growth along interfaces. Journal of the Mechanics and Physics of Solids 47 (12), 2411–2449.

Oden, J.T., 1972. Finite Elements of Nonlinear Continua. McGraw-Hill Book Company, New York.

Perrin, G., Rice, J.R., et al., 1995. Self-healing slip pulse on a frictional surface. Journal of the Mechanics and Physics of Solids 43 (9), 1461–1495.

Piva, A., Hasan, W., 1996. Effect of orthotropy on the intersonic shear crack propagation. Journal of Applied Mechanics—Transactions of the ASME 63 (4), 933–938.

Rice, J.R., Thomson, R., 1974. Ductile versus brittle behavior of crystals. Philosophical Magazine 29 (1), 73–97.

Rice, J.R., Tracey, D.M., 1969. On the ductile enlargement of voids in triaxial stress field. Journal of the Mechanics and Physics of Solids 17, 2–15.

Rosakis, P., 2001. Supersonic dislocation kinetics from an augmented Peierls model. Physical Review Letters 86 (1), 95–98.

Rosakis, A.J., 2002. Intersonic shear cracks and fault ruptures. Advances in Physics 51 (4), 1189–1257.

Rosakis, A.J., Samudrala, O., et al., 1999. Cracks faster than the shear wave speed. Science 284 (5418), 1337–1340.

Rosakis, A.J., Samudrala, O., et al., 2000. Intersonic shear crack growth along weak planes. Materials Research Innovations 3 (4), 236–243.

Samudrala, O., Huang, Y., et al., 2002. Subsonic and intersonic mode II crack propagation with a rate-dependent cohesive zone. Journal of the Mechanics and Physics of Solids 50 (6), 1231–1268.

Samudrala, O., Rosakis, A.J., 2003. Effect of loading and geometry on the subsonic/intersonic transition of a bimaterial interface crack. Engineering Fracture Mechanics 70 (2), 309–337.

Tvergaard, V., Needleman, A., 1992. Effect of crack meandering on dynamic, ductile fracture. Journal of the Mechanics and Physics of Solids 40 (2), 447–471.

Uenishi, K., Rice, J.R., 2003. Universal nucleation length for slip-weakening rupture instability under non-uniform fault loading. Journal of Geophysical Research 108 (B1), 1701–1714.

Washabaugh, P.D., Knauss, W.G., 1994. A reconciliation of dynamic crack velocity and Rayleigh-wave speed in isotropic brittle solids. International Journal of Fracture 65 (2), 97–114.

Weertman, J., 1969. Dislocations in uniform motion on slip or climb planes having periodic force law. In: Mura, T. (Ed.), Mathematical Theory of Dislocations. ASME.

Weertman, J., Weertman, J.R., 1980. Moving dislocations. In: Dislocation in Solids, vol. 3. North-Holland Publishing Co. pp. 1–60.